Journal Pre-proof

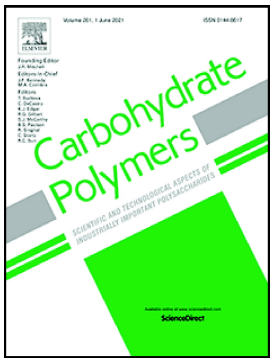

A nanocellulose-based platform towards targeted chemo-photodynamic/photothermal cancer therapy

Thu Thi Anh Do, Santiago Grijalvo, Toyoko Imae, María José Garcia-Celma, Carlos Rodríguez-Abreu

PII: S0144-8617(21)00753-0

DOI: https://doi.org/10.1016/j.carbpol.2021.118366

Reference: CARP 118366

To appear in: *Carbohydrate Polymers*

Received date: 11 December 2020

Revised date: 10 June 2021

Accepted date: 20 June 2021

Please cite this article as: T.T.A. Do, S. Grijalvo, T. Imae, et al., A nanocellulose-based platform towards targeted chemo-photodynamic/photothermal cancer therapy, *Carbohydrate Polymers* (2021), https://doi.org/10.1016/j.carbpol.2021.118366

A nanocellulose-based platform towards targeted chemo-photodynamic/photothermal cancer therapy

Thu Thi Anh Do[a], Santiago Grijalvo[b], Toyoko Imae[a,c,d]*, María José Garcia-Celma,[e] Carlos Rodríguez-Abreu[b]

[a]*Graduate Institute of Applied Science and Technology, National Taiwan University of Science and Technology, 43 Section 4, Keelung Road, Taipei 10607, Taiwan, Republic of China.*

[b]*Institute for Advanced Chemistry of Catalonia (IQAC), Spanish National Research Council (CSIC) and Networking Research Center on Bioengineering, Biomaterials and Nanomedicine (CIBER-BBN), Jordi Girona 18-26 08034, Barcelona, Spain.*

[c]*Department of Chemical Engineering, National Taiwan University of Science and Technology, 43 Section 4, Keelung Road, Taipei 10607, Taiwan, Republic of China.*

[d]*Department of Materials Science and Engineering, National Taiwan University of Science and Technology, 43 Section 4, Keelung Road, Taipei 10607, Taiwan, Republic of China.*

[e]*Department of Pharmacy and Pharmaceutical Technology and Physicochemistry, R+D+I Associated Unit to CSIC, Faculty of Pharmacy and Food Sciences. Institute of Nanoscience and Nanotechnology (IN2UB). University of Barcelona, Joan XXIII 27-31, 08028, Barcelona, Spain.*

**Corresponding author at: Graduate Institute of Applied Science and Technology, National Taiwan University of Science and Technology, Taipei 10607, Taiwan.*
E-mail address: imae@mail.ntust.edu.tw (T. Imae).

Abstract: Cellulose nanocrystals (CNCs) have advantages as drug delivery carriers because of their biocompatibility and the presence of hydroxyl groups which favor chemical modification and drug binding. The present study describes the development of novel multifunctional rod-like CNCs-based carriers as therapeutic platforms: CNCs were hybridized with folic acid for actively targeting tumor cells, carbon dots (Cdots) for both imaging and photodynamic/photothermal

treatments and doxorubicin (DOX) as an anticancer drug. Hybridized carriers displayed excellent drug-loading capacity. Moreover, Cdots-containing hybrids showed fluorescence and photosensitized singlet oxygen generation and temperature rise. Carriers exhibited pH-sensitive drug release because of changing interactions with DOX, and this release proved to be effective against *in vitro* cervical cancer cells, as evidenced by dose-dependent reduced cellular viabilities. Additionally, DOX release was promoted by light irradiation and the photodynamic behavior by reactive oxygen species was confirmed. These results demonstrate the potential of multifunctional CNCs-based carriers as platforms for multimodal photodynamic/photothermal-chemotherapy.

Keywords: cellulose nanocrystal; folic acid; carbon dots; doxorubicin; drug delivery system, photodynamic therapy

1. Introduction

Plant-based natural products have been extensively used as medicines against diseases since ancient times, and many drugs continue to be primarily extracted from natural resources. Advances in nanotechnology have made available diverse nanomaterials with potential for biomedical applications, in particular drug delivery systems (DDS). Polymer nanoparticles (e.g., ε-caprolactone, polyacrylamide), albumin, gelatin, dendrimers (e.g. poly(amido amine)), silica materials (e.g., xerogels and mesoporous silica nanoparticles), carbon nanomaterials (nanotubes and nanohorns) and magnetic nanoparticles have been commonly used in research for drug delivery (Cao, 2018; Sunasee et al., 2019). In recent times, plant-based nanostructures derived from starch, cellulose, zein, and others have been considered attractive as they are cost-effective, sustainable, and renewable materials with extraordinary physicochemical properties that are suitable for various applications (Patra et al., 2018). Cellulose is the most abundant biopolymer on the globe and it is distributed in plants, bacteria, fungi, and algae (Wondraczek & Heinze, 2015). Cellulose is composed of D-glucopyranose ring units surrounded by six hydroxyl groups and each unit is linked by β-1,4-glycosidic bonds (Karimian et al., 2019). Nano-structured cellulosic materials or nanocelluloses are divided into four main categories: bacterial nanocelluloses (BNCs), cellulose nanofibrils (CNFs), cellulose nanocrystals (CNCs), and

cellulose microfibrils (CMFs) (Plackett, Letchford, Jackson, & Burt, 2014). The main advantages of BNCs are their high porosity, low toxicity, and biocompatibility, as well as unique mechanical properties and good permeability. Therefore, BNCs can be used for wound dressing (e.g. for skin burns) and artificial blood vessels (Almeida et al., 2014). However, the main challenge for BNCs is the development of economically efficient processes for their large-scale manufacturing. CMFs and CNFs have been considered as reinforcement materials that can be used for topical administration (wound healing), bioscaffolds, and antimicrobials (Kebede, Imae, Sabrina, Wu, & Cheng, 2017; Ramaraju, Imae, & Destaye, 2015). CNCs are produced as rod-shaped or whisker-like nanoparticles, with sizes of 3-20 nm in width, and 100 to 300 nm in length, depending on cellulose sources (wood, cotton, etc.). CNCs exhibit exceptional physical (e.g. good mechanical strength) and chemical properties, high aspect ratio and large surface area (Wang, He, Zhang, Tam, & Ni, 2015). There are basically two types of surface modification of CNCs: covalent (sulfonation, esterification, silylation, etc.), and non-covalent (hydrophilic affinity, electrostatic attraction, and hydrogen bonds) (Khanjanzadeh et al., 2018; Lin & Dufresne, 2014). CNCs are generally obtained by acid hydrolysis using sulfuric acid (Lu & Hsieh, 2010). The surface hydroxyl groups of cellulose can react with sulfuric acid through an esterification reaction that produce anionic sulfate half-esters. The negatively charged surfaces of CNCs enhance colloidal stability and serve as a platform for the conjugation of numerous positively charged materials, such as cationic drug molecules, biomolecules (peptides, blood proteins), polymers, and metal nanoparticles via electrostatic interaction (Sunasee, Hemraz, & Ckless, 2016; Wang et al., 2015).

Cancer mortality is a serious concern and therefore there is a large demand for effective cancer treatments. Chemotherapy is one of the common strategies for cancer treatment, and can involve single or multiple anti-cancer drugs. However, conventional chemotherapy faces limitations such as drug resistance, lack of selectivity, and side effects such as nausea, hair loss, heart and kidney damage, among others. The fabrication of CNCs as drug delivery carriers with large surface area have allowed to control not only drug binding processes but also drug loading and release. Fluorescein-5'-isothiocyanate (FITC) has been successfully used to prepare fluorescence-labelled CNCs for bioimaging applications (Dong & Roman, 2007). In this sense, the modification of CNCs with anionic FITC and cationic rhodamine B isothiocyanate dyes has shown the ability of these materials to promote cell internalization with no indication of

cytotoxicity, suggesting that CNCs could be considered new candidates not only as bioimaging probes but also as drug carriers. (Mahmoud et al., 2010). Moreover, it has been reported that the CNCs can inhibit *E. coli* ATCC 25922 adhesion to the intestinal HT29 cell line (D'Orazio et al., 2017) and be also internalized by cancer cells in bone tumors (Colombo et al., 2015).

Wang et al. (Wang et al., 2015) reported the grafting of poly(ethyl ethylene phosphate) onto CNCs, and the encapsulation of doxorubicin (DOX) via electrostatic interaction. However, DOX-loaded nanocrystals showed lower cytotoxicity against HeLa cells in comparison with free DOX. The morphology of nanoparticles (geometry) is a key factor in biodistribution, cellular uptake, circulation time, and phagocytosis in the DDSs. Compared to spherical nanoparticles, commonly used as a nanocarrier, non-spherical nanoparticles (elongated, filament, or cylinders nanoparticles) appear to enhance the circulation time and drug loading capacity (Dong, Cho, Lee, & Roman, 2014).

Nanotechnology has enormous potential for designing multifunctional nanostructures and consequently, can help in improving cancer treatments. Herein, we report the development of multifunctional rod-like or whisker-like CNCs modified with folic acid (FA), DOX (chemotherapeutic drug) and carbon dots (Cdots) as a dual imaging-drug delivery system. Rod-shaped CNCs seem to easily penetrate into tumor cells, and improve cellular uptake (Li et al., 2019). FA is a ligand that targets folate receptors (FRs), which are overexpressed on the plasma membrane of many cancer cell types, in contrast to healthy cells that rarely express FRs (Darkhor et al., 2019). Cdots are attractive for biomedical application as they show excellent photoluminescence for bioimaging (*in vitro* and *in vivo*) and have small size and biocompatibility (Li et al., 2012; Wang et al., 2013). Moreover, it has been also reported that Cdots could be a promising candidate for photodynamic therapy because of the singlet oxygen production (Wu, Zhou, Chen, Zhang, & Wu, 2020; Zheng, Lai, & Tan, 2019). Thus, the use of Cdots is expected the wide-ranging of biomedical applications like bioimaging, photodynamic and photothermal therapies and drug delivery system.

To address these challenges, we have engineered new multifunctional nanoplatforms based on modifying the hydroxyl groups on the CNCs' surface with (3-aminopropyl) triethoxysilane (APTES) in order to improve their dispersibility. The resultant modified-CNCs were then functionalized with FA via EDC/NHS amidation followed by the incorporation of Cdots onto

CNC/APTES/FA through electrostatic interactions to produce CNC/APTES/FA/Cdots. Finally, DOX was encapsulated in both hybridized CNC/APTES/FA and CNC/APTES/FA/Cdots also by electrostatic interaction. Thus, it is expected that the extracellular pH of cancer cells may have an influence in destabilizing the electrostatic binding in our functionalized nanosystem, which would induce the release of DOX and Cdots in model cervical cancer cells. This constitutes a dual therapeutic strategy that would favor not only the *in vitro* cytotoxicity effect of an anti-cancer drug in cell culture but also photodynamic effects in the form of singlet oxygen generation. This research will provide a strategy to functionalize CNCs with the well-controlled drug release behavior, the better bioimaging property and the ability to produce singlet oxygen usable for photodynamic therapy or the temperature rise for photothermal therapy, which can extend to the multimodality treatment of cancer.

2. Experimental methods

2.1 Materials

Pulp was donated from Formosa Chemical and Fiber Corp, Taiwan. APTES and 3,3',5,5'-tetramethylbenzidine (TMB) were products from Alfa-Aesar, UK, and Dojindo, Japan, respectively. Doxorubicine·HCl and (3-(4,5-dimethylethiazol-2-yl)-2,5-diphenyltetrazolium bromide) (MTT) were purchased from Sigma-Aldrich, USA. Anthracene (99%), N-hydroxysuccinimide (NHS, 99%), 1-ethyl-3-(3-dimethylaminopropyl)-carbodiimide hydrochloride (EDC, 98%), citric acid, FA, and ethylenediamine were purchased from Acros organics, UK. Other reagents were in commercial grade. Deionized and distilled water was obtained by purification in a Millipore purification system (Yamato Millipore WT100).

2.2 Instruments

Fourier transform-infrared (FT-IR) absorption spectra were measured on a Nicolet^{TM}, Thermo Scientific, USA, using KBr pellets. X-ray diffraction (XRD) measurements were performed on a Rigaku D/Max-Ka diffractometer with CuKα (λ = 1.54184 Å) at 40 kV and 30 mA in an angle range of 2θ = 10 - 60º. Crystallinity index (CrI) values were calculated following the Segal equation, CrI (%) = $\frac{I_{(200)} - I_{am}}{I_{(200)}} \times 100$, where $I_{(200)}$ is the peak intensity at 2θ = 22.6º, and I_{am} is

the peak intensity of Bragg peak at 2θ = 18.0º of amorphous cellulose (Wu, Cao, Jiang, & Zhang, 2017). X-ray photoelectron spectroscopy (XPS) was performed on a VG Scientific ESCALAB 250, UK. The hydrodynamic diameters and zeta-potential of materials were obtained on a dynamic light scattering (DLS) analyzer (ELS-Z) from Photal Osaka Electronics, Japan. Materials were dispersed at 1 mg/ml in water or phosphate buffer solution (PBS). Ultraviolet (UV)-visible absorption spectra were measured in a Jasco V-670 spectrometer (Japan) with a 1 mm quartz cell. Fluorescence was measured with a Hitachi F-7000 fluorimeter at a scan rate of 2400 nm/min using a 1 cm quartz cell. Specimens were imaged by transmission electron microscopy (TEM) using a JEOL JEM-2100 instrument (Japan) operated at 120 kV. For a positive staining, a material mixed with phosphotungstic acid (2% (w/v) was dropped on a collodion-coated copper grid and air-dried before TEM observation. Negatively stained specimens were prepared by depositing the materials on a TEM grid, dropping phosphotungstic acid (2% (w/v)) on it, and then air-drying. Cdots dispersions were observed by high-resolution TEM (HRTEM, FEI Tecnai 20 G2 S-Twin, USA) at an acceleration voltage of 200 kV. Optical microscope images under white light (halogen lamp, LHS-H100P-1, 12 V, 100W) and in fluorescence mode (super high-pressure mercury lamp, model C-SHG1, 100 W) were taken on a Nikon-Eclipse TE 2000-U microscope (Japan).

2.3 Material preparation

Pulp (20 g) was heated in aqueous NaOH (500 mL, 4 wt%) at 70°C for 4 h to remove hemicellulose and other impurities, following by washing with water (Hastuti, Kanomata, & Kitaoka, 2018). The sodium hydroxide-treated pulp was hydrolyzed by using H_2SO_4 (500 mL, 65 wt%) at 80°C for 2 h under vigorous stirring (**Scheme 1(a)**). Then, the slurry was collected and washed thoroughly with water. Finally, the aqueous slurry was ultrasonicated for 30 min at 40 amplitude on an ultrasonic processor with a half-inch tip in an ice bath (QSONICA Q700, USA) (Lin & Dufresne, 2014), and finally water was evaporated to get a dry powder.

The modification of CNC by APTES was performed as previously reported (Khanjanzadeh et al., 2018). Briefly, APTES (10 mL) was added to water (90 mL) under vigorous stirring at pH 4 adjusted by glacial acetic acid. CNC (1 g) was added and continuously stirred at room temperature (~25°C) for 12 h, as shown in **Scheme 1(b, c)**. Then, the precipitate (CNC/APTES)

was washed twice in ethanol and once in water by centrifugation (4,000 rpm, 5 min), heated in an oven at 110°C for 30 min, purified once in ethanol and twice in water by centrifugation, and finally dried to get a powder.

For the conjugation of FA, FA (50 mg) dissolved in aqueous Na_2CO_3 solution (0.5 wt%, 20 mL) was amidated with CNC/APTES (dry powder, 100 mg) by adding EDC (43.6 mg) and NHS (26.2 mL) and stirring 48 h at room temperature (~25°C) in dark conditions (Siriviriyanun et al., 2018). The yellow precipitate (CNC/APTES/FA) was collected by centrifugation (6,000 rpm, 30 min), washed three times with water, and finally dispersed in water to form a stable dispersion.

Carbon dots (Cdots, 1:1 mole ratio of citric acid and ethylenediamine) were hydrothermally synthesized (**Scheme 1d**) (Efa & Imae, 2018). Briefly, an equimolar mixture of citric acid (1 g) and ethylenediamine (300 µL) in water (50 mL) was incubated in an autoclave at 230°C for 5 h and, subsequently, Cdots were collected as a powder and dispersed in water. The aqueous dispersion of Cdots (10 mL, 1 mg/mL) was dropped into the dispersion of CNC/APTES/FA (100 mg) in water (10 mL) and continuously stirred for 24 h (**Scheme 1(e)**). The brown precipitate (CNC/APTES/FA/Cdots) was collected by centrifugation (6,000 rpm, 30 min), washed with water, and, finally, dispersed in water for further use.

2.4 Conductometric titration

For conductometric titration, an aqueous suspension of target material (3 mL, 1 wt%) was adjusted to be acid pH by adding an adequate amount of aqueous HCl solution (1 mM) and titrated with an aqueous NaOH solution. On titration of sulfonation on CNC, a volume of an added HCl solution was 10 mL and a suspension adjusted at pH 2.76 was titrated by a 1 mM NaOH solution. The titration of amine on CNC/APTES and CNC/APTES/FA was performed using an aqueous 10 mM (= C_{NaOH}) NaOH solution for the dispersions at pH 3.54 adjusted by an aqueous HCl solution (2 mL). Then the content of target element in a relevant material can be calculated by

$$\% \text{ element} = \frac{\Delta V_{NaOH} \times C_{NaOH} \times m_{ele}}{m_{mater} \times C_{mater}} \times 100 \qquad (1)$$

where ΔV_{NaOH} is the volume difference of NaOH between two inflection points determined by the intersection of the linear regions, C_{NaOH} is the concentration of NaOH, m_{ele} is the element mass, and m_{mater} and C_{mater} are the mass and concentration of target material, respectively.

2.5 Loading and release of doxorubicin (DOX)

DOX (2 mL) at different concentrations (0.01-0.3 mg/mL) was added to a dispersion (2 mL, 0.1 mg/mL) of carriers (CNC/APTES/FA or CNC/APTES/FA/Cdots) in water and stirred for 48 h in the dark. The mixture was centrifuged (10,000 rpm, 1 h) and the supernatant was collected. The supernatant collection was repeated by adding fresh water, and the collected total supernatant was analyzed for the determination of free DOX. The loaded amount (DL) per carrier was calculated as follows (Siriviriyanun et al., 2018):

$$\text{DL (mg/mg carrier)} = \frac{Total\ mass\ DOX - Free\ mass\ DOX}{Mass\ of\ carrier} \qquad (2)$$

Amounts of total DOX in initial dispersion and free DOX in the supernatant after loading were calculated from the absorbance at a UV-visible absorption band of DOX at 480 nm using a calibration curve. All measurements were performed in triplicate and averaged.

The release of DOX from carriers was studied at physiological temperature (37°C) and two different pH (5.6 and 7.4) which correspond to the endosomal pH of cancer cells and the physiological pH of healthy cells, respectively. The DOX-loaded carriers in PBS (pH 5.6 or 7.4, 2 mL) were incubated in a water bath at 37°C. The supernatant was collected by centrifugation (10,000 rpm, 10 min), the fresh PBS (2 mL) was added to the centrifuged residue and the release experiment was continued. The released DOX was determined using the same colorimetric method used for quantifying DOX loading. The drug released was calculated as the total released amount divided by the original loaded amount. For the DOX released under light irradiation, the DOX-loaded carriers incubated in PBS at 37°C were irradiated 5 min at 2, 10 and 25 h by a light-emitting diode (LED) light (450 nm, 0.08 Wcm^{-2}, SkyFire (LumiTorch), Taiwan) and the release experiments were continued out as described above (Bao, Yin, Liu, & Chen, 2019).

2.6 Oxygen photosensitization and detection of singlet oxygen generation

The oxygen photosensitization of materials was determined from reactive oxygen species (ROS) using TMB as probe. Colorless TMB is oxidized by ROS generated from photosensitization, resulting in a blue product which was examined by absorbance at 655 nm (Wu et al., 2020). A mixture of TMB (200 $\mu g \cdot mL^{-1}$) and test materials (Cdots, CNC/APTES/FA, CNC/APTES/FA/Cdots) (10 $\mu g \cdot mL^{-1}$) was diluted with 2 mL water. Then, the mixture was

placed under (LED) light (450 nm, 0.08 Wcm^{-2}, SkyFire (LumiTorch), Taiwan) irradiation for 20 min before measuring absorbance.

To quantify the singlet oxygen generation, anthracene was used. This assay is based on the quenching of anthracene fluorescence by singlet oxygen. Emission spectra of anthracene solutions were recorded at an excitation wavelength of 320 nm (Ashjari, Dehfuly, Fatehi, Shabani, & Koruji, 2015). 1 mL of solution of anthracene in methanol (200 $\mu g \cdot mL^{-1}$) was added to 100 µL of test materials (Cdots, CNC/APTES/FA, CNC/APTES/FA/Cdots, and PPIX as a control) (200 $\mu g \cdot mL^{-1}$). After 10 min, the mixtures were irradiated for 60 min with an LED lamp (450 nm, 0.08 W cm^{-2}, SkyFire (LumiTorch), Taiwan). The rate of singlet oxygen generation was calculated from the decrease of fluorescent intensity after LED irradiation. The same experiments were performed even for CNC/APTES/FA/Cdots at LED lamp (520 nm, 0.08 W cm^{-2}, ZHNAER X-POT 26356, Germany), green laser (532 nm, 0.1 W cm^{-2}, Huonje Laser Scope, Taiwan) and red laser (650 nm, 0.1 W cm^{-2}, Huonje Laser Scope, Taiwan).

2.7 Photothermal tests

Aqueous dispersions of Cdots and CNC/APTES/FA/Cdots at Cdots concentration of 200 µg/mL were irradiated using LED (450, 650 and 808 nm, 0.1 Wcm^{-2}, ZHNAER CIMPS-X, Germany), and the temperature change of the dispersion was recorded over the period of LED irradiation using a thermometer.

2.8 *In vitro* cell cytotoxicity tests

The cytotoxicity of carriers was evaluated in cell culture using HeLa cells by the MTT (3-(4,5-dimethylethiazol-2-yl)-2,5-diphenyltetrazolium bromide) assay. In short, cells were seeded in a Dulbecco's modified Eagle's medium (DMEM) using 96-well plates at a density of 4,000 cells per well and cultured at 37°C with 5% CO_2 for 24 h. Then, aqueous dispersions of carriers at varying concentrations (0.002 to 10 $\mu g \cdot mL^{-1}$) were added and further incubated for 48 h (200 µL as a final volume). After that, DMEM was discharged and replaced by fresh DMEM solution (200 µL), and cells were additionally incubated for 2 h. The cells were then subjected to the MTT assay. MTT (15 µL, 0.5 $mg \cdot ml^{-1}$ in PBS) was added in each well and incubated for 2 h. After the medium was removed, the dark-blue formazan crystal in each well was dissolved in dimethyl sulfoxide (200 µL). The absorbance of the resulting cell dispersions was measured at

560 nm using a microplate reader (Labsystem, Multiskan, Ascent, Model 354, Finland). The cell viability in percentage was calculated and compared to untreated cells. The cytotoxicity of reference materials to HeLa cells at pH 7.4 was also evaluated using the MTT assay. The IC_{50} values were determined by GraphPad Prism Software.

3. Results and discussion

3.1 Preparation and characterization of CNCs-based hybridized carriers

CNC-based drug delivery systems were synthesized and hybridized by combining APTES, FA, and Cdots, as illustrated in **Scheme 1(a)**, following three step reactions: (i) APTES was chemically grafted onto CNCs through Si-O-C bonds, (ii) FA was bound by an amidation reaction on CNC/APTES, and (iii) Cdots were adsorbed on CNC/APTES/FA.

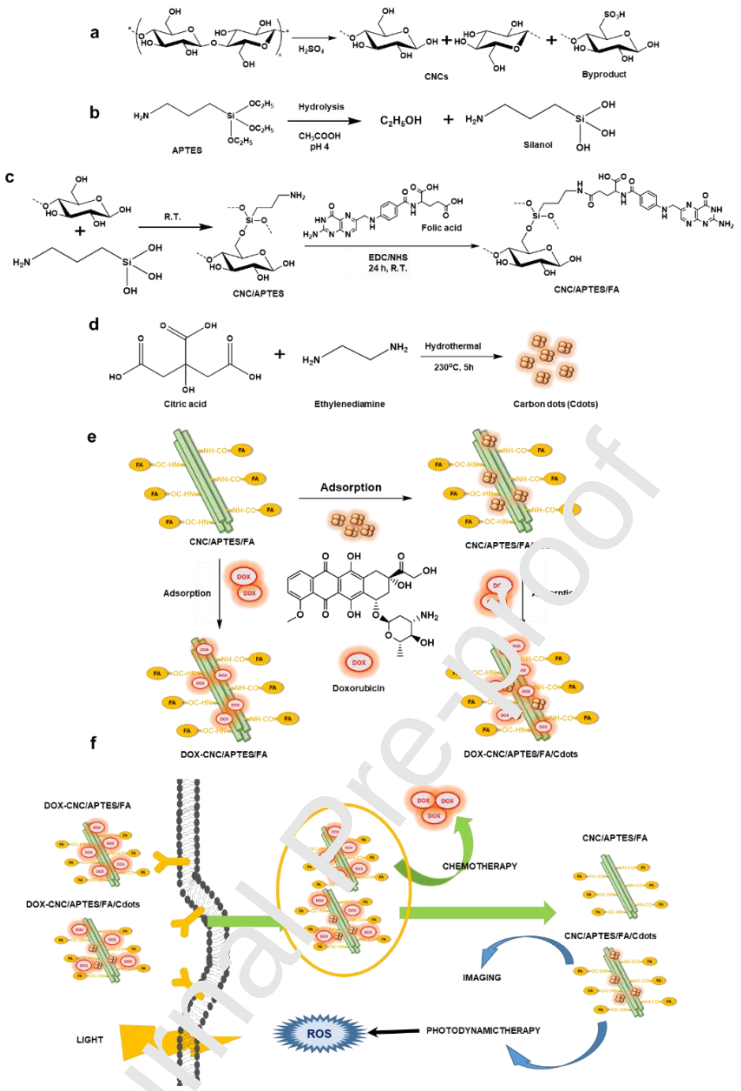

Scheme 1. Strategy for the synthesis of hybridized materials. (a) Acid hydrolysis of pulp, (b) hydrolysis of APTES, (c) chemical binding of hydrolyzed APTES onto CNCs and amidation binding of FA onto CNC/APTES, (d) synthesis of Cdots, (e) adsorption of DOX onto CNC/APTES/FA and CNC/APTES/FA/Cdots, and (f) chemo- and photo-therapeutic actions of CNC/APTES/FA and CNC/APTES/FA/Cdots in Hera cells.

TEM images of positively and negatively stained CNCs are shown in **Fig. 1(A1, A2).** CNCs in positive staining appear as rod-like or whisker-like particles, regardless of surface functionalization (Baek, Hanif, Cho, Kim, & Um, 2013), in contrast to cellulose nanofibers (CNF) that are thinner and longer (Ujihara, Hsu, Liou, & Imae, 2018). In comparison with positively stained TEM images, the negatively stained TEM images seem to be rather

homogeneous strings. The effect of preparation procedure on TEM textures has been previously discussed (Imae, Takahashi, & Muramatsu, 1992). Note that Cdots cannot be observed in **Fig.1(A1, A2)** since they are very small and required higher magnification to be imaged. The size of Cdots was estimated to be ~1 nm from HRTEM **(Supplementary Information Fig. S1(a))**.

IR spectra and band assignments for the synthesized materials are included in **Fig. 1(B), Fig. S1(b, c)** and **Table S1**. For CNCs, the bands at about 1430 and 1373 cm^{-1}, respectively, are ascribed to the symmetric CH_2 bending vibration and the overlapped –C-H and –C-O bending vibrations of the aromatic rings in polysaccharides (Khanjanzadeh et al., 2018). The bands at 1058 and 1012 cm^{-1} are assigned to –C-O stretching vibrations of secondary and primary alcohol groups of cellulose and hemicellulose, and the vibration band at 902 cm^{-1} is attributed to the glycoside bonds which are symmetric in polysaccharides and correspond to the β-glucosidic linkage between glucose units in cellulose (Lopes, Garcia, & Souza, 2018). The spectrum of CNC/APTES also shows the characteristic absorption bands of CNCs and an additional band at around 1550 cm^{-1}, assigned to –NH bending vibration of primary amine, suggesting that APTES were successfully bonded onto CNCs surface (Khanjanzadeh et al., 2018). The CNC/APTES/FA spectrum shows the main bands of both FA, and CNC/APTES and confirms the conjugation of FA to modified CNCs (CNC/APTES) by using EDC/NHS as a coupling reagent. The bands at 1628 and 1540 cm^{-1} are assigned to the amide bonding vibrations of $–CONH_2$, which confirms the conjugation of FA onto the CNC/APTES surface. The spectrum of Cdots in **Fig. S1(c)** shows bands at 3392, 1653, 1554, and 1492 cm^{-1}, attributed to –OH, –C=O, –C=C bonds of the aromatic ring and –C-N bonds, respectively. However, there is almost no difference between the FT-IR spectra of CNC/APTES/FA and CNC/APTES/FA/Cdots samples because these CNCs-based hybridized carriers contain almost the same functionalized groups (hydroxyl, carbonyl, and nitrogen-containing groups).

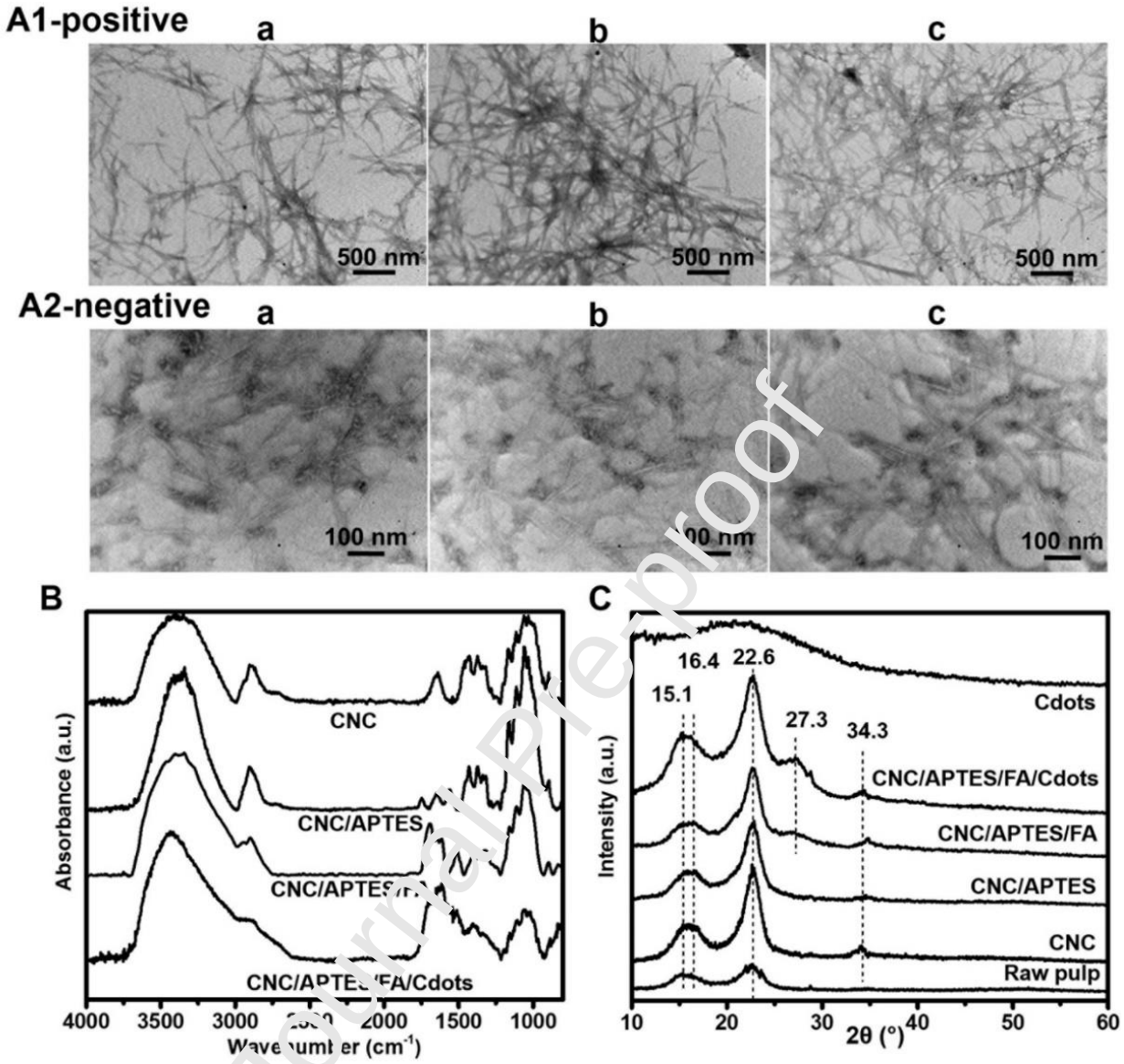

Fig. 1. TEM images after (A1)-positive staining and (A2)-negative staining of (a) CNC, (b) CNC/APTES/FA, (c) CNC/APTES/FA/Cdots. (B) FT-IR absorption spectra, and (C) XRD patterns of raw pulp, CNC, CNC/APTES, CNC/APTES/FA and CNC/APTES/FA/Cdots and Cdots.

Fig. 1(C) displays the XRD patterns of raw pulp, CNC, CNC/APTES, CNC/APTES/FA, CNC/APTES/FA/Cdots and Cdots. The diffractogram of raw pulp showed peaks at 15.1º, 16.4º and 22.6º assigned to (110), (110), and (200) crystallographic planes, respectively, of monoclinic cellulose Iβ lattice (Taipina, Ferrarezi, Yoshida, & Gonçalves, 2012). Bragg peaks of CNC at

22.6º and 34.3º of (200) and (004) planes, respectively, became sharper, because of the degradation of amorphous and disordered regions of cellulose during the acidic hydrolysis. CNC/APTES showed the same XRD pattern as neat CNC, indicating no influence of APTES on crystallinity. The XRD pattern of CNC/APTES/FA revealed a new peak at 27.3º which comes from FA crystals (Beagan et al., 2017), although this peak was not indexed. The XRD of CNC/APTES/FA/Cdots showed a similar pattern to that of CNC/APTES/FA although the peak at 27.3º was more intense. The XRD analysis of Cdots resulted in a very broad diffraction peak around 23º corresponding to the (002) graphite lattice plane, being typical of very small particles (2-3 nm) (Geleta & Imae, 2021). The calculated CrI of raw pulp was 59.9%, and it was lower than CNC (76.5%). CrI values of CNC/APTES, CNC/APTES/FA and CNC/APTES/FA/Cdots were 70.1%, 68.0% and 66.0%, respectively (Chekini et al., 2019). The decrease of CrI values upon addition of APTES, FA and Cdots suggests that the grafting of additives on CNC reduces crystallinity (Mohd et al., 2016; Wu et al., 2017). Thus, the XRD results indicate that chemical modification did not significantly affect the crystalline structure of CNCs but changed the degree the crystallinity.

Materials were further characterized by XPS. Full survey XPS spectra (**Fig. 2(A))** revealed the existence of C 1s (286 eV) and O 1s (533 eV) for all materials and of Si (100 eV), and N 1s (400 eV) only for CNC/APTES and CNC/APTES/FA. In high resolution and deconvoluted **Fig. 2(B)**, C 1s spectra of CNC displayed two peaks at 284.15 and 285.53 eV assigned to sp^3C and sp^2C (C-H and C-C), respectively, a peak 286.87 eV assigned to C-OH, and a peak at 288.77 eV assigned to C-O-C. (Alanis et al. 2019). The deconvoluted O1s spectra showed two peaks located at 532.13 and 533.33 eV corresponding to C-OH and C-O-C, respectively (Pereira et al., 2014).

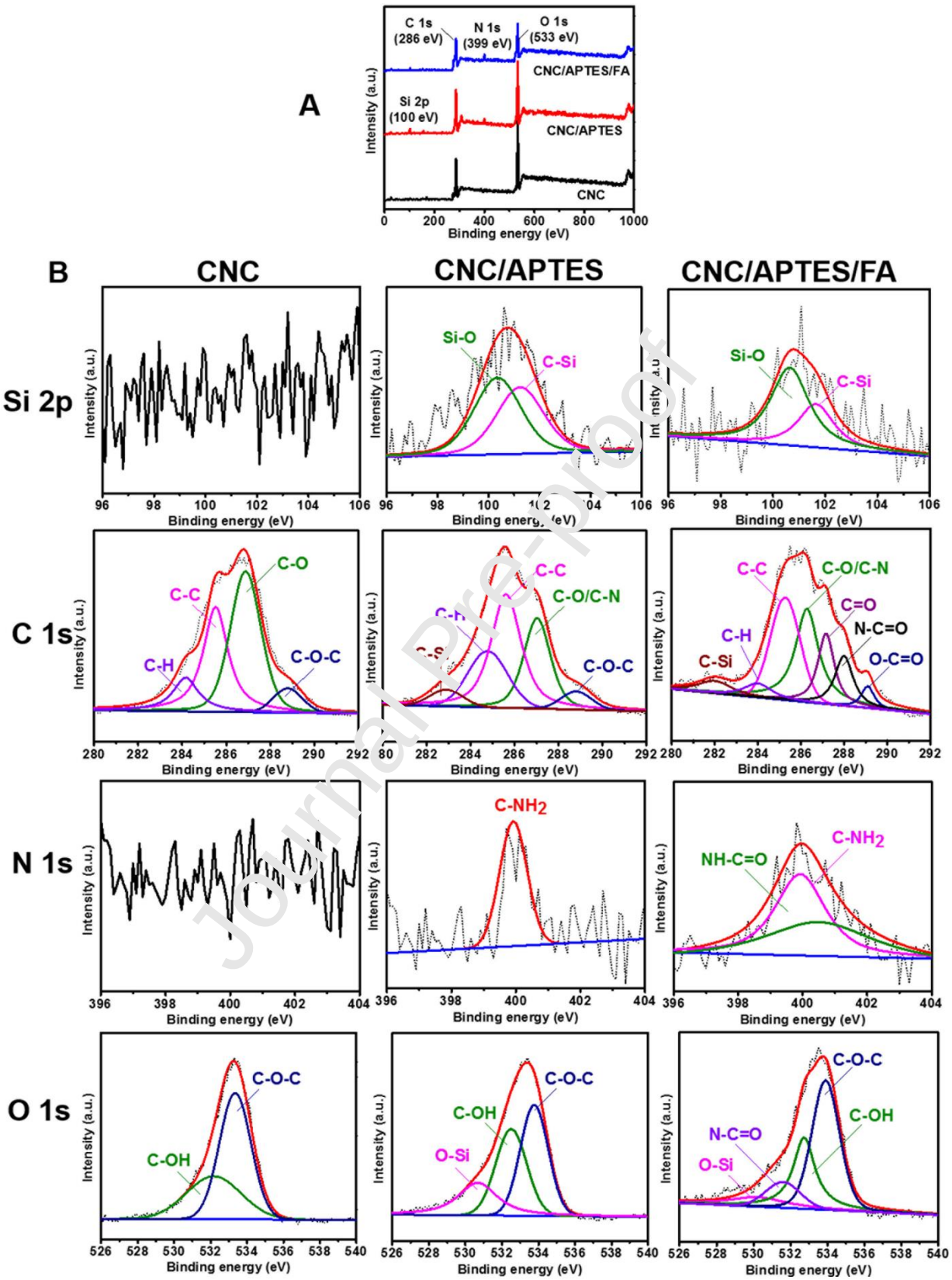

Fig. 2. (A) XPS survey scan and (B) high resolution and deconvoluted spectra of CNC, CNC/APTES, and CNC/APTES/FA.

Peaks at 284.62, 285.59, 287.06 and 288.78 eV in the deconvoluted C 1s spectra of CNC/APTES can be assigned to CNC, but a peak at 287.06 eV was overlapped with the one corresponding to C-N binding energy (Liu, Duan, Qian, Zhou, & Yuan, 2013). A new peak at 282.86 eV corresponds to C-Si bond. In addition to C-OH bond (532.51 eV) and C-O-C bond (533.77 eV) of CNC, the deconvoluted O 1s spectra of CNC/APTES show a new peak at 530.67 eV assigned to O-Si bond. CNC/APTES displayed one N 1s peak at 399.9[illegible] eV assigned to C-NH_2. The deconvoluted Si 2p show two peaks located at 100.37 and 101.[illegible]5 eV, which correspond to Si-O and C-Si, respectively (Ruiz-Cañas, Quintero, Corredor, Marriquez, & Romero Bohórquez, 2020). These XPS results confirm the binding of APTES on CNC (Gueye et al., 2016).

The deconvoluted C 1s spectra of CNC/APTES/FA showed the same peaks as those of CNC/APTES and located at 282.25, 283.94, 285.13, and 286.30 eV. In addition, new peaks at 287.14, 288.02 and 289.15 eV can be assigned to C=O, N-C=O and COOH bonds of FA (Ekiz et al., 2011; Kwon et al., 2018). Two deconvoluted N1s peaks at 399.92 and 400.50 eV were assigned to NH/NH_2 and N-C=O, respectively, of FA (Arcot, Lundahl, Rojas, & Laine, 2014). The O 1s spectrum of CNC/APTES/FA was deconvoluted into three peaks (530.23, 532.74, and 533.91 eV) of CNC/APTES and a new peak at 531.61 eV corresponding to COOH bound to FA. The deconvoluted Si 2p peaks on CNC/APTES/FA were consistent with those of CNC/APTES, confirming the existence of siloxane bonds produced by the binding of APTES on CNC. Thus, the binding of FA on CNC/APTES was proved by these XPS results.

Table 1 lists the elemental composition of CNC, CNC/APTES and CNC/APTES/FA calculated by integration of deconvoluted XPS peaks using CasaXPS software. The content of elemental S in CNCs, CNC/APTES and CNC/APTES/FA was 0.57, 0.13 and 0.10 atomic %, respectively, which are quite small. The content of elemental N of CNC/APTES was 3.72 atomic % and it increased to 6.08 atomic % after FA conjugation. On the other hand, the content (3.61 atomic %) of elemental Si in CNC/APTES decreased to 2.02 atomic % in CNC/APTES/FA. Then the calculated O/C ratio was 0.61 % for CNCs but decreased with APTES and FA.

Table 1. Elemental composition (by atomic %) and O/C atomic ratio obtained from XPS analysis for CNC, CNC/APTES and CNC/APTES/FA.

Sample	C	O	N	S	Si	O/C ratio
CNC	61.59	37.84	0	0.57	0	0.61
CNC/APTES	65.04	27.56	3.72	0.13	3.61	0.42
CNC/APTES/FA	69.27	22.54	6.08	0.10	2.02	0.33

Elemental analysis can also be carried out by conductometric titration. Titration curves of sulfonation on CNC are shown in **Fig. 3(A).** Initially, there is a decrease in conductivity with adding NaOH because of the neutralization of free HCl in the suspension. Then there is a change in the conductivity trend with a slight increase caused by deprotonation of sulfonic acid. Finally, there is a steep increase in conductivity due to the presence of excess NaOH. The volume of NaOH utilized for deprotonation was ΔV_{NaOH} = 3.452 ± 0.015 mL; from this value, the sulfur content was estimated as 0.383 ± 0.018 wt%. This content is small alike a value from XPS analysis (Table 1) and similar to that reported by Beck et al (0.54-0.62 %) (Beck, Méthot, & Bouchard, 2015). Thus, the contamination of sulfonated-CNC unit is negligible, although it is expected that the sulfur content will depend on sample preparation (reaction time, acid concentration) and purification before titration.

The binding of APTES and FA on CNC was also analyzed by conductometric titration of target elemental N (amine-related), as shown in **Fig. 3(B, C)**. The estimated nitrogen contents were 3.379 ± 0.012 % and 5.502 ± 0.010 %, for CNC/APTES and CNC/APTES/FA, respectively. These values are comparable to the results (**Table 1**) obtained from XPS analysis. The conductometric titration curve for CNC/APTES, as seen in **Fig. 3(B), s**hows three stages. In the conductivity-decreasing first stage (black dotted line), added NaOH neutralizes free HCl. In the second stage (blue dotted line) protonated primary amine groups are neutralized. In the last stage (red dotted line), conductivity increases with increasing NaOH ionic species. In contrast, for CNC/APTES/FA, the conductometric titration (**Fig. 3(C))** proceeded through four stages. The two stages in the middle correspond to neutralization of protonated primary and secondary amine groups of FA in CNC/APTES/FA (Zhao et al., 2017). Thus, the total N content of CNC/APTES/FA is higher than that of CNC/APTES.

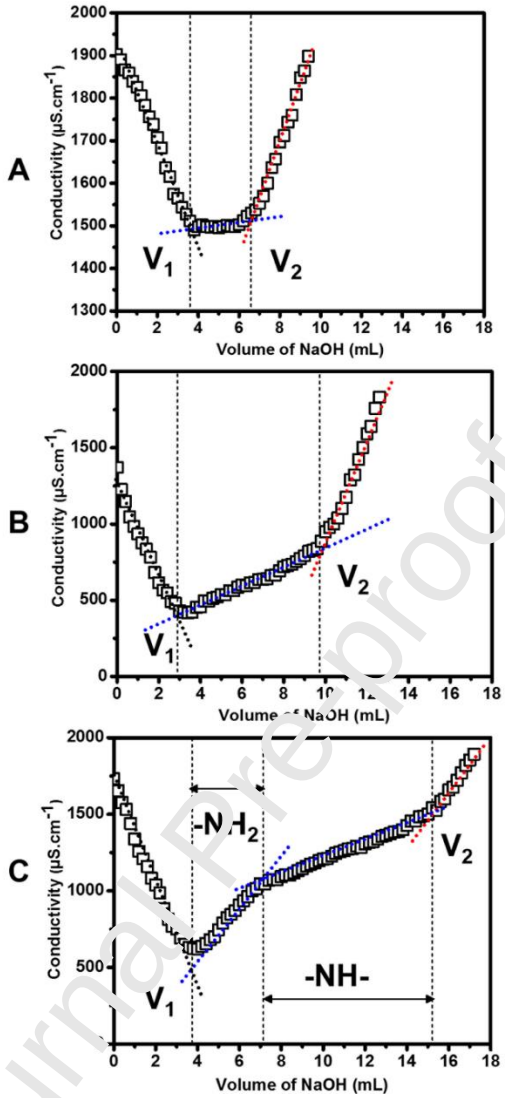

Fig. 3. Conductometric titration curves of aqueous suspensions of (A) CNC, (B) CNC/APTES/FA and (C) CNC/APTES/FA/Cdots.

The size of CNCs-based carriers in water was evaluated by DLS. The equivalent hydrodynamic diameter of CNCs ranged from 100 to 300 nm (179.4 ± 16.1 nm). Interestingly, the equivalent hydrodynamic diameter of these nanomaterials changed little when they were modified using APTES, FA or Cdots, as seen in **Fig. S1(d)**. The zeta-potential values of CNCs and their hybridized materials are shown in **Fig. S1(e)**. CNC/APTES displayed an isoelectric point at around pH 4 caused by the contribution of the protonated amine groups of APTES bound on CNCs. The zeta potential became negative (-15 to -35 mV) after conjugation with FA whereas amphoteric Cdots did not affect much the zeta potential values of CNC/APTES/FA.

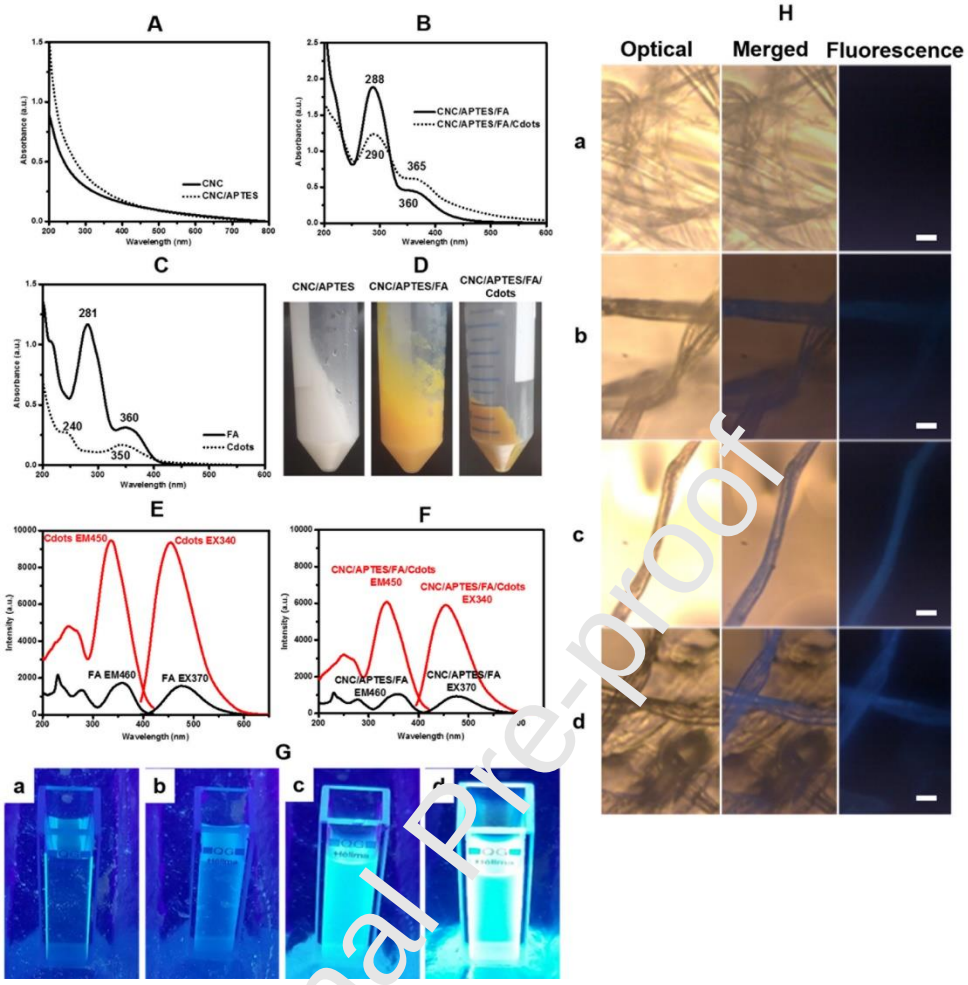

Fig. 4. UV-visible absorption spectra of (A) CNC and CNC/APTES, (B) CNC/APTES/FA and CNC/APTES/FA/Cdots, and (C) FA and Cdots. (D) Pictures of CNC/APTES, CNC/APTES/FA and CNC/APTES/FA/Cdots. Fluorescence spectra of (E) FA (black line) and Cdots (red line) and (F) CNC/APTES/FA (black line) and CNC/APTES/FA/Cdots (red line). (G) Photoluminescence phenomena of aqueous dispersions of (a) FA, (b) CNC/APTES/FA, (c) CNC/APTES/FA/Cdots and (d) Cdots under fluorescence light. (H) Microscopic images at optical, merged and fluorescence modes of (a) cotton, (b) CNC/APTES/FA-treated cotton, (c) CNC/APTES/FA/Cdots-treated cotton, and (d) Cdots-treated cotton fibrils (Scale bar: 10 µm).

As seen in the UV-visible absorption spectra **(Fig. 4(A))**, both CNC and CNC/APTES have no absorption bands in the UV-visible region. However, the UV-visible absorption spectrum of CNC/APTES/FA (**Fig. 4(B))** shows two bands at 288 and 355 nm assigned to π-π^* and n-π^* transitions, respectively, of pterine ring in FA molecule (Dong et al., 2014). These bands of

CNC/APTES/FA were slightly shifted as compared to the bands (281 and 360 nm) of pristine FA (**Fig. 2(C)**). This shift may relate to the production of an amide bond between FA and CNC/APTES (Chakraborty, Roy, Bairi, & Nandi, 2012). The FA content in CNC/APTES was approximately 13.9 wt% as determined from the absorbance band at 360 nm (**Fig S2(a)**). The UV-visible absorption spectrum of Cdots showed two bands at 245 and 350 nm, respectively, corresponding to a π–π* transition of aromatic –C=C–, and –C-C– bonds in the sp^2 domains of graphitic structure, and an n–π* transition of –C=O, –C-N or –C-OH bonds in carboxyl or amine groups in the sp^3 domains of Cdots, as seen in **Fig. 4(C)**. However, after the conjugation of Cdots on CNC/APTES/FA, the absorption bands (290 and 365 nm, **Fig. 4(B)**) were closer to those of CNC/APTES/FA than to those of pristine amphoteric Cdots because of the low Cdots content (12.8 wt%), (quantified by the absorbance at 350 nm) (**Fig S2(b)**) (Chakraborty et al., 2012). There are also macroscopic changes in the samples after the functionalization of our nano-carriers with FA and Cdots. The CNC/APTES sample appeared as a white gel that changed to yellow after FA was added, and the resultant yellow CNC/APTES/FA gel became brownish with the addition of Cdots as shown in **Fig. 4(D)**.

As shown in **Fig. 4(A)**, CNC, and CNC/APTES did not show any UV-visible absorption bands and they did not have any fluorescent properties either. As shown in **Fig. 4(E)**, the maximum excitation and emission wavelengths are located at 370 and 460 nm for FA (Juzeniene, Thu Tam, Iani, & Moan, 2013). These bands were also observed for CNC/APTES/FA, which confirmed the successful conjugation of FA as seen in **Fig. 4(F)**. On the other hand, Cdots showed much more intense fluorescence as compared to FA. The fluorescence bands (an excitation band at 340 nm and an emission band at 450 nm) of Cdots were also observed for CNC/APTES/FA/Cdots.

The increase of fluorescence upon addition of Cdots is also evident macroscopically, as shown in **Fig. 4(G)**. CNC/APTES/FA/Cdots displayed strong fluorescence emission as well as free Cdots, but this behavior was different from free FA and CNC/APTES/FA, which presented very weak emission. The prepared materials also showed fluorescence when adsorbed on substrates such as cotton fibrils, as seen **Fig. 4(H)** (Wang, Imae, & Miki, 2007)**.** CNC/APTES/FA/Cdots-treated cotton fibrils and Cdots-treated cotton fibrils showed strong blue emission. These results are attributed to the strong luminescence property of Cdots (Etefa, Imae, & Yanagida, 2020; Geleta & Imae, 2021), suggesting potential use as fluorescence markers.

3.2 Characterization of DOX-loaded on CNCs-based hybridized carriers

The zeta-potentials of DOX and DOX-loaded hybridized carriers were determined at pH 5.6 and 7.4 in PBS (see **Fig. 5(A))**. At pH 5.6, DOX and DOX-loaded hybridized carriers have a positive charge, however, DOX-loaded hybridized carriers are negatively charged except for DOX at pH 7.4. These changes might be caused by the electrostatic interaction of positively charged DOX molecules with negatively charged hybridized carriers. These results suggest that the DOX-loaded CNC-based hybridized carriers can maintain their negative surface charge in the blood (pH 7.4), and change to a positive surface charge in acidic environment after internalization in tumor cells. In addition, the reduction of the negative charge might result in longer circulation times and reduced uptake by macrophages (Khandelia, 2015). In **Fig. 5(B)**, the UV-visible spectra of DOX-CNC/APTES/FA and DOX-CNC/APTES/FA/Cdots at pH 5.6 and 7.4 in PBS shows a new band at 480 nm attributed to DOX. Moreover, the pictures in **Fig. 5(C)** show that DOX-CNC/APTES/FA/Cdots hybridized carriers were darker than DOX-CNC/APTES/FA due to the anchoring of Cdots on the surface. As seen in **Fig. S2(c, d),** free DOX, DOX-loaded hybridized carriers (CNC/APTES/FA and CNC/APTES/FA/Cdots) in PBS at pH 5.6 and 7.4 (excitation wavelength: 480 nm) showed the characteristic emission bands of DOX (560 and 590 nm) (Motlagh, Parvin, Ghasemi, & Atyabi, 2016). These results indicate the successful loading of DOX onto these hybridized carries.

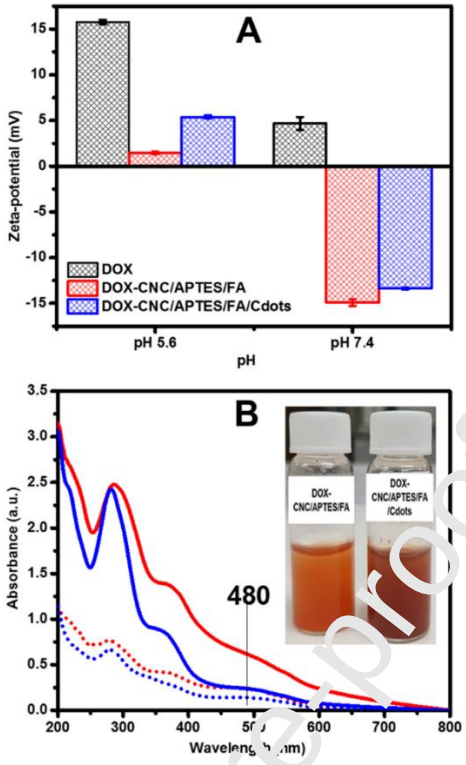

Fig. 5. (A) Zeta-potential of DOX (black), DOX-CNC/APTES/FA (red) and DOX-CNC/APTES/FA/Cdots (blue) at pH 5.6 and 7.4. (B) UV-visible absorption spectra of DOX-CNC/APTES/FA (red), DOX-CNC/APTES/FA/Cdots (blue) at pH 5.6 (solid line) and 7.4 (dotted line). Inset pictures are suspensions of DOX-CNC/APTES/FA and DOX-CNC/APTES/FA/Cdots.

3.3 Loading and release of doxorubicin (DOX) on CNC/APTES/FA and CNC/APTES/FA/Cdots

DOX was loaded on the surface of CNCs-based hybridized carriers (CNC/APTES, CNC/APTES/FA and CNC/APTES/FA/Cdots) at pH 7.0. DOX loading on CNC/APTES/FA and CNC/APTES/FA/Cdots was higher than on CNC/APTES as shown in **Fig. 6(A)**. This could be due to the presence of more available binding sites in CNC/APTES/FA and CNC/APTES/FA/Cdots and an increase in the number of their hydrogen bonding and π-π stacking interactions with DOX besides the presence of electrostatic interactions of CNC/APTES with DOX (Sunasee et al., 2016; Wang et al., 2015). The loading at neutral pH is expected to be

more effective than in acidic or basic conditions since carboxylate and amine groups in the carrier and DOX are normally charged (Siriviriyanun et al., 2018) and then electrostatic interaction is favored (Leisner & Imae, 2003). As seen in **Fig. 6(A)**, the DOX loading increased with concentration of DOX until saturation plateau is reached. The DOX loading capacity at a 0.15 mg/ml DOX concentration on CNC/APTES, CNC/APTES/FA and CNC/APTES/FA/Cdot was 0.714 (15.7 %), 1.034 (25.2 %) and 1.053 mg/mg of carrier (27.3 %), respectively. It is fascinating that the present loading capacities are much superior to 8 % reported for rod-like cellulose/cis-aconityl-DOX prodrug (Li et al., 2019) and 19.4 % for cellulose-nanocrystal-based folate (Li et al., 2019).

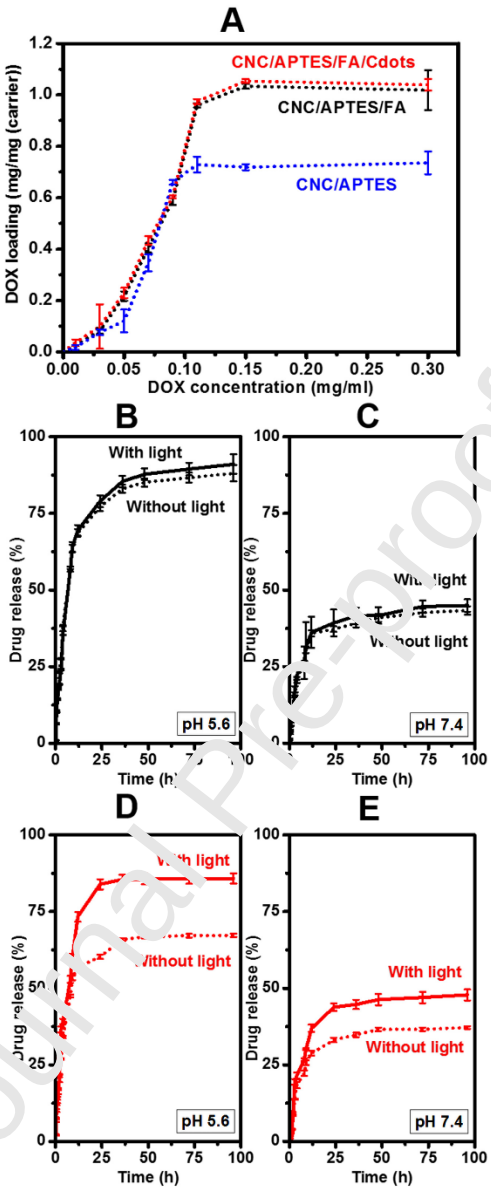

Fig. 6. (A) DOX loading on CNC/APTES (blue), CNC/APTES/FA (black) and CNC/APTES/FA/Cdots (red); and DOX release profiles from (B, C) DOX-CNC/APTES/FA and (D, E) DOX-CNC/APTES/FA/Cdots at pH 5.6 and pH 7.4 (dotted line) without light radiation and (solid line) with light radiation.

The drug release from the hybridized carriers at 37°C (physiological temperature) was studied in PBS at pH 5.6 and 7.4, corresponding to the endosomal pH of cancer cells and the physiological

pH of healthy cells, respectively. As shown in **Fig. 6(B-E),** the drug release at pH 5.6 is much larger than that at pH.7.4. The DOX release at pH 5.6 for DOX-CNC/APTES/FA and DOX-CNC/APTES/FA/Cdots increased with time and reached 88.1 ± 2.7 % and 67.3 ± 0.6 %, respectively, after 96 h-incubation. Meanwhile, 43.4 ± 1.4 % (DOX-CNC/APTES/FA) and 37.2 ± 0.5 % (DOX-CNC/APTES/FA/Cdots) of DOX were released at pH 7.4 for the same incubation times. The sustained release of DOX at neutral pH may have a major advantage since some side effects might be prevented (Wang et al., 2015).

In the presence of the light irradiation **(**see **Fig. 6(B-E))**, the DOX release from DOX-CNC/APTES/FA at both pH 5.6 and 7.4 was slightly higher than that in the absence of light irradiation, although these differences were within experimental error. In contrast, the drug release of DOX-CNC/APTES/FA/Cdots at pH 5.6 and 7.4 increased significantly upon light irradiation, reaching 85.8 ± 1.6 % and 47.8 ± 1.8 % respectively. These results suggest that Cdots act as a photosensitizer that generate thermal energy locally upon light irradiation, causing a bond cleavage and triggering DOX release.

3.4 Singlet oxygen generation performance of materials

The singlet oxygen generation was studied using Protoporphyrin IX (PPIX) as a control since it is a model photosensitizing molecule for various applications (Ashjari et al., 2015). The oxygen photosensitization properties of the materials were confirmed by using TMB as a ROS probe, which changes to blue upon oxygen photosensitization with a characteristic absorption band at 655 nm, as seen in **Fig. 7(A, B)** and **Fig. S3** (Wu et al., 2020). The singlet oxygen productivity of the materials was measured using anthracene, as a chemical probe for the detection of singlet oxygen ($^1O_2$), as seen in **Fig. 7(C-H) and Fig. S4(a)** (Ashjari et al., 2015). The amount of anthracene consumption (indicated by the fluorescence decay) correlates with the amount of singlet oxygen produced. The emission spectrum of anthracene shows the characteristic four excitation bands at 388, 403, 426, and 450 nm (**Fig. S4(b)**).

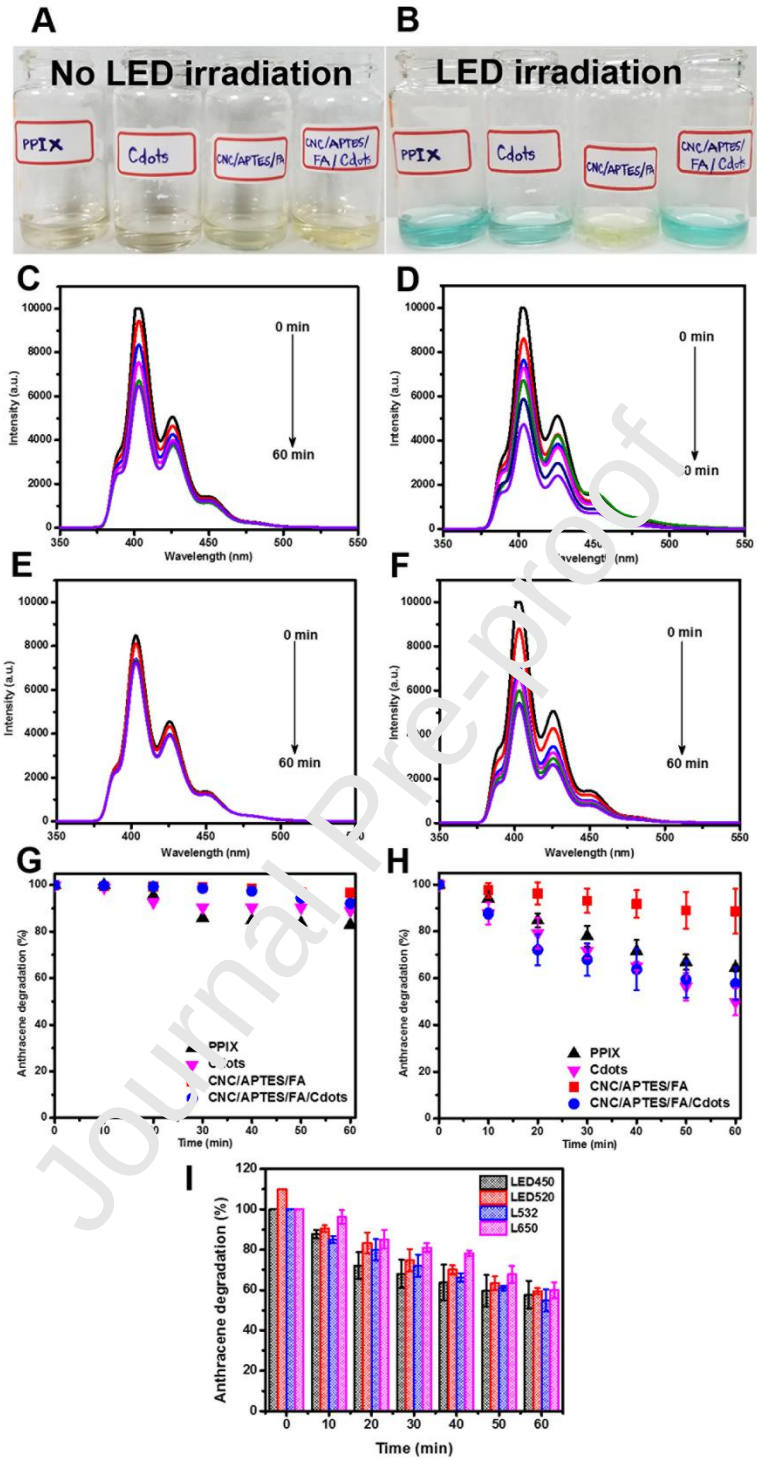

Fig. 7. Pictures of materials in TMB solution (A) without and (B) with LED irradiation. (C-F) the emission spectra of (C) PPIX, (D) Cdots, (E) CNC/APTES/FA, and (F) CNC/APTES/FA/Cdots in anthracene solutions after LED irradiation for every 10 min (black

line: 0 min, red line: 10 min, blue line: 20 min, pink line: 30 min, green line: 40 min, dark blue line: 50 min and violet line: 60 min). The anthracene degradation of these materials (G) without and (H) with LED irradiation. (I) Anthracene degradation of CNC/APTES/FA/Cdots under irradiation with (black) LED (450 nm), (red) LED (520 nm), (blue) green laser (532 nm) and (pink) red laser (650 nm).

In the presence of PPIX as well as Cdots, the fluorescence intensity of anthracene dramatically decreased under LED light irradiation (60 min), and the efficiency of singlet oxygen generation of Cdots as a photosensitizing molecule was determined (see **Fig. 7(C, D))**. However, in the absence of LED light irradiation (60 min), the fluorescence intensity of anthracene showed little change (**Fig. S4(c, d)**). The emission spectra at 320 nm excitation wavelength of CNC/APTES/FA were essentially unchanged during 60 min without or with LED light, as seen in **Fig. 7(E)** and **Fig. S4(e)**. FA, a poor singlet oxygen sensitizer, hardly produced singlet oxygen in comparison with other pterin derivates such as 6-formylpterin, 6-carboxypterin, neopterin, and biopterin). The fluorescence quantum yield of FA was much inferior when compared to other pterin derivatives due to the presence of substituted long-chain, which could behave as an internal quencher to fluorescence, increasing of the deactivation (without radiation) of the singlet excited state. Consequently, the intersystem-crossing turns out ineffective, and causes FA to be a poor singlet oxygen photosensitizer (Juzeniene et al., 2013). Moreover, CNC/APTES/FA/Cdots also showed a high efficiency in singlet oxygen generation in comparison with CNC/APTES/FA, as seen in **Fig. 7(F)** and **Fig. S4(f)**. Notably, the fluorescence decay of anthracene after 60 min in the presence of Cdots under LED light irradiation was much higher (ca. 50 %) than in the absence of irradiation (dark condition) (ca. 10 %), as seen in **Fig. 7(G, H)**, illustrating that the singlet oxygen generation mostly occurred by photosensitizing (Zheng et al., 2019). These results demonstrate the high potential of CNC/APTES/FA/Cdots carriers for photodynamic application in comparison with CNC/APTES/FA carrier. In addition, the dependence of light source on singlet oxygen generation was examined. It can be noticed from **Fig. 7(I)** that the anthracene degradation was higher by laser than by LED, when it was compared between LED of 520 nm and laser of 532 nm, but the degradation at lower light wavelength was superior to the degradation at higher light

wavelength, although the difference of degradation under LED of 450 nm and laser of 650 nm was at most 15 %. Thus, an LED light of 450 nm was preferable in the present work.

3.5 Photothermal effect of materials

To improve the suggestion described above that Cdots may act as a photosensitizer to generate thermal energy upon light irradiation, the temperature rise upon the light irradiation was examined. Aqueous dispersions of Cdots and CNC/APTES/FA/Cdots were irradiated using LED (450, 650 and 808 nm), and the temperature change of the dispersion was recorded over the period of laser irradiation using a thermometer. As seen in **Fig. 8(A)**, the temperature increment of water was at most 2^{o}C even by any LED lights under 10 min irradiation, but the temperature of both Cdots and CNC/APTES/FA/Cdots dispersions increased by irradiation of an LED. Furthermore, the temperature increase depended on LED wavelength (about 6^{o}C, 11 - 12^{o}C and up to 14^{o}C under LED 450 nm, 650 and 808 nm, respectively). **Fig. 8(B)** suggested that the increasing temperature was mainly effected by the concentration of Cdots. These results indicate that the photothermal efficacy of Cdots and CNC/APTES/FA/Cdots is mainly dominated by Cdots, irradiation time, wavelength of LED and concetration of Cdots or Cdots-incorporated materials. Although the lower wavelength light (LED 450 nm) was advantageous for singlet oxygen generation, the light source of higher wavelength (650 and 808 nm) in near IR spectral region was effective for photothermal performance, being preferable on therapy because of deeper light penetration into tissues.

Polythiophene phenylpropionic acid conjugated Cdots were a promising agent for photothermal therapy (Ge et al., 2015). The ideal photothermal agents for in vivo applications required high absorption coefficient that should run into the biological transparency window, i.e. 650 – 950 nm, where light tends to have the maximum depth of penetration in tissues. Thus, a new type of S, N-doped Cdots had intense absorption bands in the red to near IR region and showed near IR fluorescence and high photothermal conversion efficiency (Bao et al., 2018). Fluorescent polydopamine passivated Cdots also exhibited the excellent effectiveness of photothernal therapy in vitro test (Bai et al., 2018). These reports support the valid performance of Cdots as a photothernal trigger.

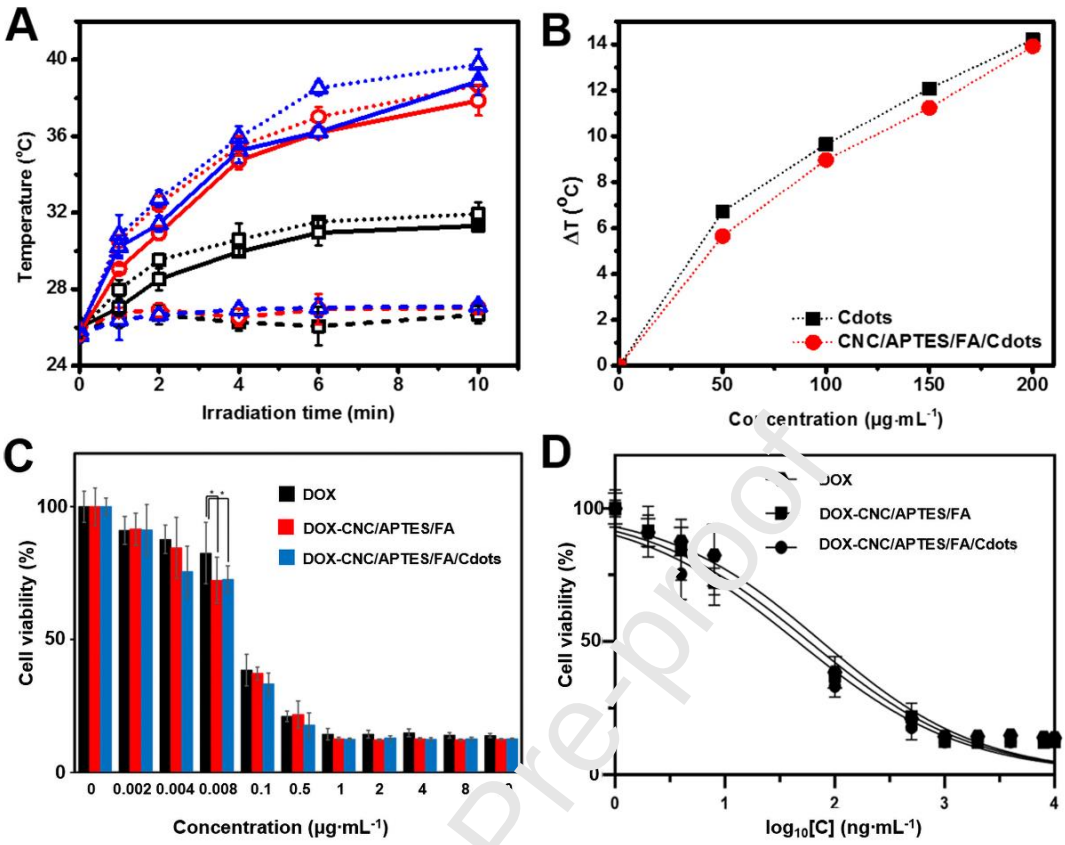

Fig. 8. (A) Temperature rise of (dashed line) water, (dotted line) an aqueous Cdots dispersion and (solid line) an aqueous CNC/APTES/FA/Cdots dispersion at Cdots concentration of 200 μg/mL during 10 min irradiation by (black square) LED (450nm), (red circle) LED (650nm) and (blue triangle) LED (808nm), and (B) temperature rise difference of aqueous Cdots and CNC/APTES/FA/Cdots dispersions at different concentrations under LED (808nm) irradiation for 10 min. (C) Cell viability and (D) IC_{50} of HeLa cells treated with DOX, DOX-CNC/APTES/FA and DOX-CNC/APTES/FA/Cdots at different concentrations of DOX after 48 h-incubation. Data are average values of triple independent experiments.

3.6 *In vitro* cell cytotoxicity tests

We studied the release and toxicity of DOX in cell culture. According to **Scheme 1(f)**, we expected that DOX release from CNC-based hybridized carriers (CNC/APTES/FA and CNC/APTESFA/Cdots) would be higher in acidic conditions. This could have a positive

outcome if these nanoplatforms were used to target cancer cells. Besides the effect of pH, the presence of FA as a ligand in CNC may result in high affinity to tumor surface-receptors (FRs), which may tend to enhance the cellular uptake of CNCs-based carriers. Moreover, the rod-like morphology and specific surface chemical properties of the present carriers might increase cellular uptake and consequently promote cancer cell death (Li et al., 2018; Li et al., 2019). Herein, the cytotoxicity of DOX-CNC/APTES/FA and DOX-CNC/APTES/FA/Cdots was studied in the presence of cervical cancer cells at various concentrations of DOX after 48h-incubation using the colorimetric MTT assay. These toxicity results were compared to free DOX as a control. As shown in **Fig. 8(C)**, both DOX-CNC/APTES/FA and hybridized DOX-CNC/APTES/FA/Cdots displayed an efficacy similar to free DOX i.e. approximately 10% at 0.002 $\mu g \cdot mL^{-1}$ and 90% at 1 $\mu g \cdot mL^{-1}$, when compared to free DOX as positive control. The IC_{50} (half-inhibition to cell growth) values of these two carriers are shown in **Fig. 8(D)** and **Table S2**. Interestingly, we found that IC_{50} values for free DOX (IC_{50} = 76.26 $ng \cdot mL^{-1}$) were higher than that DOX-CNC/APTES/FA (IC_{50} = 58.8 $ng \cdot mL^{-1}$) and DOX-CNC/APTES/FA/Cdots (IC_{50} = 46.01 $ng \cdot mL^{-1}$).

4. Conclusions

Material (CNC/APTES/FA/Cdots) with potential application in therapy made of CNCs hybridized with FA and Cdots has been synthesized and successfully characterized. In addition, DOX has been loaded as a model chemotherapeutic drug. The drug release was pH-sensitive, i.e. it increased when pH was changed from 7.4 to 5.6. This pH-responsive behavior along with high drug loading makes this system a promising candidate for controlled and targeted drug delivery. In addition, the drug release increased under light irradiation, indicating that the conjugation with photothermal procedure is useful to release drug and that the utilization of drugs with side effects can be diminished. In fact, the temperature rise under LED light irradiation was detected, suggesting that the weakened interaction between DOX and carrier (CNC/APTES/FA/Cdots) promotes the release of DOX. Moreover, ROS and singlet oxygen generation of CNC/APTES/FA/Cdots was confirmed, which may be promising the photodynamic therapy. Finally, toxicity results showed that DOX-loaded CNCs-based hybridized carriers exhibit a potential anticancer activity against cervical cancer cells. In view of these results, CNCs may be

envisaged as promising nanoplatforms to be used both in chemical and photodynamic/photothermal therapies against cancer. Based on the present reports relating to the possible multimodal therapeutic application, the biomedical research of the relative materials should be performed.

Acknowledgements

C.R. is grateful to the financial support from the Spanish Ministry of Economy and Competitiveness (CTQ2017-84998-P project), the European Regional Development Fund, Generalitat de Catalunya (2017SGR01778) and Centro de Investigación Biomédica en Red de Bioingeniería, Biomateriales y Nanomedicina (CIBER-BBN). Support from the I-LINK 1188 project (CSIC) is also acknowledged. T.T.A.D. thanks the National Taiwan University of Science and Technology for kind financial support through a student scholarship.

References

Alanis, A., Valdés, J. H., María Guadalupe, P.-V., Lopez, R., Mendoza, R., Mathew, A. P., Díaz de León, R., & Valencia, L. 2018. Plasma surface-modification of cellulose nanocrystals: a green alternative towards mechanical reinforcement of ABS. ***RSC Adv.***, 9(30): 17417-17424.

Almeida, I. F., Pereira, T., Silva, N. H. C. S., Gomes, F. P., Silvestre, A. J. D., Freire, C. S. R., Sousa Lobo, J. M., & Costa, P. C. 2014. Bacterial cellulose membranes as drug delivery systems: An in vivo skin compatibility study. ***Eur. J. Pharm. Biopharm.***, 86(3): 332-336.

Arcot, L. R., Lundahl, M., Rojas, O. J., & Laine, J. 2014. Asymmetric cellulose nanocrystals: thiolation of reducing end groups via NHS–EDC coupling. ***Cellulose***, 21(6): 4209-4218.

Ashjari, M., Dehfuly, S., Fatehi, D., Shabani, R., & Koruji, M. 2015. Efficient functionalization of gold nanoparticles using cysteine conjugated protoporphyrin IX for singlet oxygen production in vitro. ***RSC Adv.***, 5(127): 104621-104628.

Baek, C., Hanif, Z., Cho, S.-W., Kim, D., & Um, S. 2013. Shape Control of Cellulose Nanocrystals via Compositional Acid Hydrolysis. ***J. Biomed. Nanotechnol.***, 9: 1293-1298.

Bai, Y., Zhang, B., Chen, L., Lin, Z., Zhang, X., Ge, D., Shi, W., & Sun, Y. 2018. Facile One-Pot Synthesis of Polydopamine Carbon Dots for Photothermal Therapy. ***Nanoscale Res. Lett.***, 13(1): 287-295.

Bao, X., Yuan, Y., Chen, J., Zhang, B., Li, D., Zhou, D., Jing, P., Xu, G., Wang, Y., Holá, K., Shen, D., Wu, C., Song, L., Liu, C., Zbořil, R., & Qu, S. 2018. In vivo theranostics with near-infrared-emitting carbon dots—highly efficient photothermal therapy based on passive targeting after intravenous administration. ***Light Sci. Appl.***, 7(1): 91-101.

Bao, Y., Yin, L., Liu, L., & Chen, L. 2019. Acid sensitive ROS- triggered dextran- based drug delivery system for advanced chemo- photodynamic synergistic therapy. ***J. Biomed. Mater. Res., Part A***, 108(1):148-156.

Beagan, A., Aouak, T., Aljuhaiman, L., Al-Odayni, A.-B., Saeed, W., & Ouladsmane, M. 2017. Poly(2-hydroxyethylmethacrylate-*co*-2-folate ethylmethacrylate) and Folic acid/Poly(2-hydroxyethylmethacrylate) Solid Solution: Preparation and Drug Release Investigation, ***Polym. Plast. Technol. Eng.***, 56(18): 1997-2018.

Beck, S., Méthot, M., & Bouchard, J. 2015. General procedure for determining cellulose nanocrystal sulfate half-ester content by conductometric titration. ***Cellulose***, 22(1): 101-116.

Cao, Y. 2018. Applications of cellulose nanomaterials in pharmaceutical science and pharmacology. ***Express Polym. Lett.***, 12(9): 768-780.

Chakraborty, P., Roy, B., Bairi, P., & Nandi, A. K. 2012. Improved mechanical and photophysical properties of chitosan incorporated folic acid gel possessing the characteristics of dye and metal ion absorption. ***J. Mater. Chem.***, 22(38): 20291-20298.

Chekini, M., Prince, E., Zhao, L., Mundoor, H., Smalyukh, I., & Kumacheva, E. 2019. Chiral Carbon Dots Synthesized on Cellulose Nanocrystals. ***Adv. Opt. Mater.***, 8: 1901911-1901919.

Colombo, L., Zoia, L., Violatto, M. B., Previdi, S., Talamini, L., Sitia, L., Nicotra, F., Orlandi, M., Salmona, M., Recordati, C., Bigini, P., & La Ferla, B. 2015. Organ Distribution and Bone Tropism of Cellulose Nanocrystals in Living Mice. ***Biomacromolecules***, 16(9): 2862-2871.

D'Orazio, G., Munizza, L., Zampolli, J., Fiorella, M., Zoia, L., Fusi, P., Di Gennaro, P., & La Ferla, B. 2017. Cellulose nanocrystals are effective in inhibiting host cell bacterial adhesion. ***J. Mater. Chem. B***, 5(34): 7018-7020.

Darkhor, P., Narmani, A., Rezvani, M., Farnood, B., Mohammadnejad, J., Amini, B., Refahi, S., & Abdi Goushbolagh, N. 2019. Folic acid functionalized nanoparticles as pharmaceutical carriers in drug delivery systems. ***Drug Dev. Res.***, 80(4):404-424.

Dong, S., Cho, H. J., Lee, Y. W., & Roman, M. 2014. Synthesis and Cellular Uptake of Folic Acid-Conjugated Cellulose Nanocrystals for Cancer Targeting. ***Biomacromolecules***, 15(5): 1560-1567.

Dong, S., & Roman, M. 2007. Fluorescently Labeled Cellulose Nanocrystals for Bioimaging Applications. ***J. Am. Chem. Soc.***, 129(45): 13810-13811.

Efa, M. T., & Imae, T. 2018. Hybridization of carbon-dots with ZnO nanoparticles of different sizes. ***J. Taiwan Inst. Chem. Eng.***, 92: 112-117.

Ekiz, F., Oğuzkaya, F., Akin, M., Timur, S., Tanyeli, C., & Toppare, L. 2011. Synthesis and application of poly-SNS-anchored carboxylic acid: a novel functional matrix for biomolecule conjugation. ***J Mater. Chem.***, 21(33): 12337-12343.

Etefa, H. F., Imae, T., & Yanagida, M. 2020. Enhanced Photosensitization by Carbon Dots Co-adsorbing with Dye on p-Type Semiconductor (Nickel Oxide) Solar Cells. ***ACS Appl. Mater. Interfaces***, 12(16): 18596-18608.

Ge, J., Jia, Q., Liu, W., Guo, L., Liu, Q., Lan, M., Zhang, H., Meng, X., & Wang, P. 2015. Red-Emissive Carbon Dots for Fluorescent, Photoacoustic, and Thermal Theranostics in Living Mice. ***Adv. Mater.***, 27: 4169-4177.

Geleta, T. A., & Imae, T. 2021. Nanocomposite Photoanodes Consisting of p-NiO/n-ZnO Heterojunction and Carbon Quantum Dot Additive for Dye-Sensitized Solar Cells. ***ACS Appl. Nano Mater.***, 4(1): 236-249.

Gueye, M., Gries, T., Noël, C., Migot-Choux, S., Bulou, S., Lecoq, E., Choquet, P., Kutasi, K., & Belmonte, T. 2016. Interaction of (3-Aminopropyl)triethoxysilane with Pulsed Ar–O2 Afterglow: Application to Nanoparticles Synthesis. ***Plasma Chem. Plasma Process.***, 36(4): 1031-1050.

Hastuti, N., Kanomata, K., & Kitaoka, T. 2018. Hydrochloric Acid Hydrolysis of Pulps from Oil Palm Empty Fruit Bunches to Produce Cellulose Nanocrystals. ***J. Polym. Environ.***, 26(9): 3698-3709.

Imae, T., Takahashi, Y., & Muramatsu, H. 1992. Formation of fibrous molecular assemblies by amino acid surfactants in water. ***J. Am. Chem. Soc.***, 114(9): 3414-3419.

Juzeniene, A., Thu Tam, T. T., Iani, V., & Moan, J. 2013. The action spectrum for folic acid photodegradation in aqueous solutions. ***J. Photochem. Photobiol., B***, 126: 11-16.

Karimian, A., Parsian, H., Majidinia, M., Rahimi, M., Mir, S. M., Samadi Kafil, H., Shafiei-Irannejad, V., Kheyrollah, M., Ostadi, H., & Yousefi, B. 2019. Nanocrystalline cellulose: Preparation, physicochemical properties, and applications in drug delivery systems. ***Int. J. Biol. Macromol.***, 133: 850-859.

Kebede, M. A., Imae, T., Sabrina, Wu, C.-M., & Cheng, K.-B. 2017. Cellulose fibers functionalized by metal nanoparticles stabilized in dendrimer for formaldehyde decomposition and antimicrobial activity. ***Chem. Eng. J.***, 311: 340-347.

Khandelia, R. 2015. Gold Nanocluster Embedded Albumin Nanoparticles for Two-Photon Imaging of Cancer Cells Accompanying Drug Delivery. ***Small***, 2015: 4075-4081.

Khanjanzadeh, H., Behrooz, R., Bahramifar, N., Gindl-Altmutter, W., Bacher, M., Edler, M., & Griesser, T. 2018. Surface chemical functionalization of cellulose nanocrystals by 3-aminopropyltriethoxysilane. ***Int. J. Biol. Macromol.***, 106: 1288-1296.

Kwon, B., Park, J., Jeong, W., Jeong, S., Ryu, H. S., Paoprasert, P., Park, S. Y., & In, I. 2018. Assembly of chemically reduced graphene oxide with folic acid functionalized with pyrene moieties and electrochemical sensing of folate receptors. ***Carbon Lett.***, 27: 26-34.

Leisner, D., & Imae, T. 2003. Polyelectrolyte Behavior of an Interpolyelectrolyte Complex Formed in Aqueous Solution of a Charged Dendrimer and Sodium Poly(l-glutamate). ***J. Phys. Chem. B***, 107(47): 13158-13167.

Li, N., Liang, X., Wang, L., Li, Z., Li, P., Zhu, Y., & Song, J. 2012. Biodistribution study of carbogenic dots in cells and in vivo for optical imaging. ***J. Nanopart. Res.***, 14(10): 1177-1185.

Li, N., Lu, W., Yu, J., Xiao, Y., Liu, S., Gan, L., & Huang, J. 2018. Rod-like cellulose nanocrystal/cis-aconityl-doxorubicin prodrug: A fluorescence-visible drug delivery system with enhanced cellular uptake and intracellular drug controlled release. ***Mater. Sci. Eng., C***, 91: 179-189.

Li, N., Zhang, H., Xiao, Y., Huang, Y., Xu, M., You, D., Lu, W., & Yu, J. 2019. Fabrication of Cellulose-Nanocrystal-Based Folate Targeted Nanomedicine via Layer-by-Layer Assembly with Lysosomal pH-Controlled Drug Release into the Nucleus. ***Biomacromolecules***, 20(2): 937-948.

Lin, N., & Dufresne, A. 2014. Surface chemistry, morphological analysis and properties of cellulose nanocrystals with gradiented sulfation degrees. ***Nanoscale***, 6(10): 5384-5393.

Liu, Z., Duan, X., Qian, G., Zhou, X., & Yuan, W. 2013. Eco-friendly one-pot synthesis of highly dispersible functionalized graphene nanosheets with free amino groups. ***Nanotechnology***, 24: 045609-045614.

Lopes, J., Garcia, R., & Souza, N. 2018. Infrared spectroscopy of the surface of thermally-modified teak juvenile wood. ***Maderas, Cienc. tecnol.***, 20(4):737-746.

Lu, P., & Hsieh, Y.-L. 2010. Preparation and properties of cellulose nanocrystals: Rods, spheres, and network. ***Carbohydr. Polym.***, 82(2): 329-336.

Mahmoud, K. A., Mena, J. A., Male, K. B., Hrapovic, S., Kamen, A., & Luong, J. H. T. 2010. Effect of Surface Charge on the Cellular Uptake and Cytotoxicity of Fluorescent Labeled Cellulose Nanocrystals. ***ACS Appl. Mater. Interfaces***, 2(10): 2924-2932.

Mohd, N. H., Ismail, N. F. H., Zahari, J. I., Wan Fathilah, W. F. b., Kargarzadeh, H., Ramli, S., Ahmad, I., Yarmo, M. A., & Othaman, R. 2016. Effect of Aminosilane Modification on Nanocrystalline Cellulose Properties. ***J. Nanomater.***, 2016: 4804271-4804278.

Motlagh, N. S. H., Parvin, P., Ghasemi, F., & Atyabi, F. 2016. Fluorescence properties of several chemotherapy drugs: doxorubicin, paclitaxel and bleomycin. ***Biomed. Opt. Express***, 7(6): 2400-2406.

Patra, J. K., Das, G., Fraceto, L. F., Campos, E. V. R., Rodriguez-Torres, M. d. P., Acosta-Torres, L. S., Diaz-Torres, L. A., Grillo, R., Swamy, M. K., Sharma, S., Habtemariam, S., & Shin, H.-S. 2018. Nano based drug delivery systems: recent developments and future prospects. ***J. Nanobiotechnol.***, 16(1): 71-103.

Pereira, P., Voorwald, H., Cioffi, M. O., Silva, M., Rego, A. M., Ferraria, A., & Pinho, M. 2014. Sugarcane bagasse cellulose fibres and their hydrous niobium phosphate composites: Synthesis and characterization by XPS, XRD and SEM. ***Cellulose***, 21: 641-652.

Plackett, D., Letchford, K., Jackson, J., & Burt, H. 2014. A review of nanocellulose as a novel vehicle for drug delivery. ***Nordic Pulp Pap. Res. J.***, 29: 105-118.

Ramaraju, B., Imae, T., & Destaye, A. G. 2015. Ag nanoparticle-immobilized cellulose nanofibril films for environmental conservation. ***Appl. Catal., A***, 492: 184-189.

Ruiz-Cañas, M. C., Quintero, H. I., Corredor, L. M., Manrique, E., & Romero Bohórquez, A. R. 2020. New Nanohybrid Based on Hydrolyzed Polyacrylamide and Silica Nanoparticles: Morphological, Structural and Thermal Properties. ***Polymers***, 12(5):1152-1166.

Siriviriyanun, A., Tsai, Y. J., Yoon, S. H., Kiew, S. F., Imae, T., Kiew, L. V., Looi, C. Y., Wong, W. F., Lee, H. B., & Chung, L. Y. 2018. Cyclodextrin- and dendrimer-conjugated graphene oxide as a nanocarrier for the delivery of selected chemotherapeutic and photosensitizing agents. ***Mater. Sci. Eng., C***, 89: 307-315.

Sunasee, R., Carson, M., Despres, H. W., Pacherille, A., Nunez, K. D., & Ckless, K. 2019. Analysis of the Immune and Antioxidant Response of Cellulose Nanocrystals Grafted with β-Cyclodextrin in Myeloid Cell Lines. ***J. Nanomater.***, 2019: 1-9.

Sunasee, R., Hemraz, U., & Ckless, K. 2016. Cellulose nanocrystals: A versatile nanoplatform for emerging biomedical applications. ***Expert Opin. Drug Deliv.***, 13(9):1243-1256.

Taipina, M., Ferrarezi, M., Yoshida, I., & Gonçalves, M. 2012. Surface modification of cotton nanocrystals with a silane agent. ***Cellulose***, 20: 217-226.

Ujihara, M., Hsu, M.-H., Liou, J.-Y., & Imae, T. 2018. Hybridization of cellulose nanofiber with amine-polymers and its ability on sick house syndrome gas decomposition. ***J. Taiwan Inst. Chem. Eng.***, 92: 106-111.

Wang, D., Imae, T., & Miki, M. 2007. Fluorescence emission from PAMAM and PPI dendrimers. ***J. Colloid Interface Sci.***, 306(2): 222-227.

Wang, H., He, J., Zhang, M., Tam, K. C., & Ni, P. 2015. A new pathway towards polymer modified cellulose nanocrystals via a "grafting onto" process for drug delivery. ***Polym. Chem.***, 6(23): 4206-4209.

Wang, Q., Huang, X., Long, Y., Wang, X., Zhang, H., Zhu, R., Liang, L., Teng, P., & Zheng, H. 2013. Hollow luminescent carbon dots for drug delivery. ***Carbon***, 59: 192-199.

Wondraczek, H., & Heinze, T. 2015. Cellulosic Biomaterials. In K. G. Ramawat, & J.-M. Mérillon (Eds.), ***Polysaccharides: Bioactivity and Biotechnology***: 289-328. Cham: Springer International Publishing.

Wu, S., Zhou, R., Chen, H., Zhang, J., & Wu, P. 2020. Highly efficient oxygen photosensitization of carbon dots: the role of nitrogen doping. ***Nanoscale***, 12(9): 5543-5553.

Wu, Y., Cao, F., Jiang, H., & Zhang, Y. 2017. Preparation and characterization of aminosilane-functionalized cellulose nanocrystal aerogel. ***Mater. Res. Express***, 4(8): 085303-085309.

Zhao, F., Repo, E., Song, Y., Yin, D., Hammouda, S. B., Chen, L., Kalliola, S., Tang, J., Tam, K. C., & Sillanpää, M. 2017. Polyethylenimine-cross-linked cellulose nanocrystals for highly efficient recovery of rare earth elements from water and a mechanism study. ***Green Chem.***, 19(20): 4816-4828.

Zheng, X. T., Lai, Y. C., & Tan, Y. N. 2019. Nucleotide-derived theranostic nanodots with intrinsic fluorescence and singlet oxygen generation for bioimaging and photodynamic therapy. ***Nanoscale Adv.***, 1(6): 2250-2257.

Credit Author Statement

The authors declare that they have no known competing financial interests or personal relationships that could have appeared to influence the work reported in this paper.

Graphical abstract

A nanocellulose-based platform towards targeted chemo-photodynamic cancer therapy

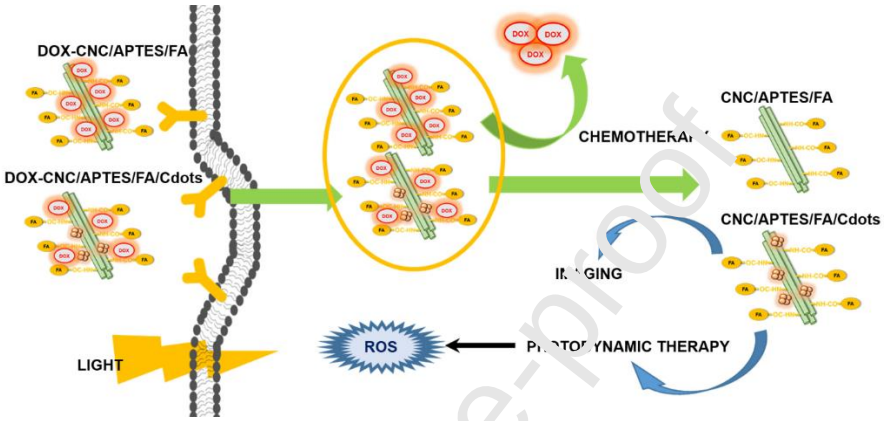

Hightlights

- Multifunctional cellulose nanocrystal (CNC) drug delivery carriers were fabricated.
- CNCs bear folic acid to target tumor cells and Cdots for singlet oxygen generation.
- Doxorubicin was loaded in the carriers as a model chemotherapeutic drug.
- Carriers display pH-responsive behavior for controlled and targeted drug delivery.
- Carriers showed potential anticancer activities against cervical cancer cells.